

# Optical detection of chemical warfare agents and toxic industrial chemicals: Simulation

Michael E. Webber and Michael Pushkarsky

*Pranalytica, Inc., 1101 Colorado Avenue, Santa Monica, California 90401*

C. Kumar N. Patel<sup>a)</sup>

*Pranalytica, Inc., 1101 Colorado Avenue, Santa Monica, California 90401*

*and Department of Physics and Astronomy, University of California, Los Angeles, California*

(Received 11 November 2004; accepted 10 March 2005; published online 23 May 2005)

We present an analysis of optical techniques for the detection of chemical warfare agents and toxic industrial chemicals in real-world conditions. We analyze the problem of detecting a target species in the presence of a multitude of interferences that are often stochastic and we provide a broadly applicable technique for evaluating the sensitivity, probability of false positives (PFP), and probability of false negatives (PFN) for a sensor through the illustrative example of a laser photoacoustic spectrometer (L-PAS). This methodology includes (1) a model of real-world air composition, (2) an analytical model of an actual field-deployed L-PAS, (3) stochasticity in instrument response and air composition, (4) repeated detection calculations to obtain statistics and receiver operating characteristic curves, and (5) analyzing these statistics to determine the sensor's sensitivity, PFP, and PFN. This methodology was used to analyze variations in sensor design and ambient conditions, and can be utilized as a framework for comparing different sensors. © 2005 American Institute of Physics. [DOI: 10.1063/1.1900931]

## I. INTRODUCTION

The terrorist events of September 11, 2001, subsequent anthrax mailings, and the earlier 1995 Tokyo subway sarin attack by the Aum Shinrikyo cult has heightened worldwide awareness of the catastrophic social impact of potential large-scale attacks using chemical warfare agents (CWAs), and has exposed the critical need for the reliable, unambiguous, and early detection of trace CWAs and toxic industrial chemicals (TICs) in the air. Despite the fact that all countries worldwide are signatories to the Chemical Weapons Convention,<sup>1</sup> which bans the use of CWAs, the U.S. defense establishments have considered their use possible and thus have developed battlefield sensors for the ambient detection of CWAs to protect troops. However, CWA sensors suitable for civilian use in places such as airports, railroad stations, large public and private office buildings, theaters, sports arenas, etc., have received much less attention. Such civilian sensors may be required to meet different performance criteria than those deployed in battlefields. For example, in public settings there is a need for the early detection of CWAs so that parts of buildings can be rapidly isolated or evacuated, while a low probability of false positives (PFP) is a necessity to avoid the adverse economic impact caused by false alarms leading to unnecessary evacuations.

This paper presents an analysis of the capability of optical techniques, using laser photoacoustic spectroscopy (L-PAS) as an example, for the detection of CWAs and TICs by explicitly incorporating the stochastic nature of sensor noise characteristics and interferences in a real-world situation. This analysis, based on a model developed to simulate an

actual trace gas sensor, yields theoretical receiver operational characteristic (ROC) curves, which include quantitative sensitivity, selectivity, PFP, and PFN as a function of instrument noise characteristics, spectrometer spectral coverage, and air composition. Thus, this paper provides a universal road map for optimizing the performance of trace gas sensors in the presence of interferences and for performing useful inter-comparisons of different techniques.

We use L-PAS to illustrate the analytical methodology by (1) simulating real-world air that represents a complicated mix of potential interferences, (2) creating an analytical model of the L-PAS sensor, (3) incorporating stochasticity to the model by adding random noise proportional the instrument's precision and varying interference concentrations, (4) simulating the operation of the sensor model by performing repeated sample calculations to yield useful statistics and ROC curves, and then (5) analyzing these statistics to determine the sensor's replicate precision (sensitivity), PFP (selectivity), and probability of false negatives (PFN) (reliability).

A brief background on photoacoustic IR spectroscopy is included in Sec. II. Section III describes the simulation model developed to evaluate the sensor performance, comprising a model of realistically contaminated air, a model of actual sensor performance, and quantitative spectral libraries. Section IV presents the results of a L-PAS sensor performance simulation for CWA detection. Section V extends the analysis to predict performance of notional sensors with different operational characteristics and different levels of air contamination, thus, providing "scaling laws" for optical sensors and permitting sensor performance evaluations in extreme situations. Section VI summarizes the results and provides conclusions.

<sup>a)</sup>Author to whom correspondence should be addressed; electronic mail: patel@pranalytica.com

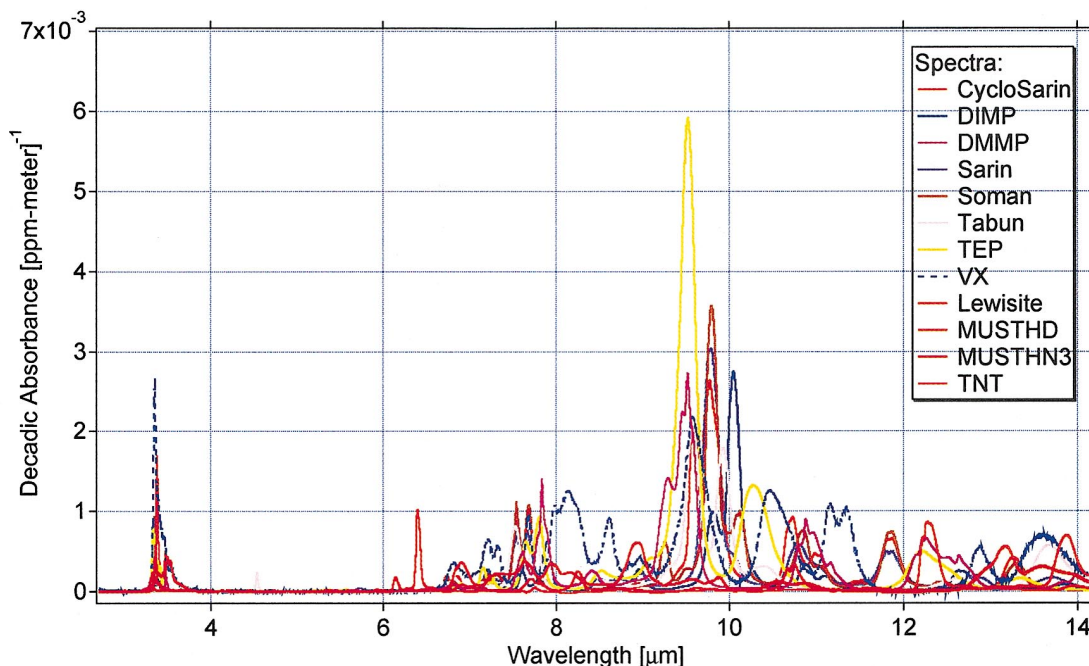


FIG. 1. (Color) Infrared-absorption spectra for CWAs, mustards, and TNT.

## II. OPTICAL DETECTION OF TRACE GASES

IR-absorption spectroscopy is a powerful tool for trace gas detection because a vast majority of polyatomic molecules including CWAs, TICs, and explosives absorb light in the wavelength region from 3 to 14  $\mu\text{m}$ . Figure 1 shows<sup>2</sup> the IR spectra of nerve gases, mustards, and TNT, illustrating that the most prominent features for many species of interest lie between 3 and 11.5  $\mu\text{m}$ , and Table I lists some of the pertinent species that can be detected in different wavelength regions.

### A. Sensor requirements

When evaluating an optical detection technology, the following performance characteristics are important:

TABLE I. CWAs, TICs, and explosives that can be detected in specific spectral regions.

<b>9–11.5 <math>\mu\text{m}</math></b>	
CWAs	Lewisite, nitrogen mustard (H-N3), sulfur mustard (HD), 4-dithiane, diisopropyl methylphosphonate (DIMP), dimethyl methylphosphonate (DMMP), isoamyl alcohol, methylphosphonic difluoride (DIFLUOR), cyclosarin (GF), sarin (GB), soman (GD), tabun (GA), VX, triethyl phosphate (TEP), 2-diisopropylaminoethanol (DIPAE)
TICs	Ammonia, arsine, boron trichloride, ethylene oxide, nitric acid
<b>4–9 <math>\mu\text{m}</math></b>	
CWAs	Mustard (H-N3), sulfur mustard (HD), 4-dithiane
TICs	Boron trifluoride, carbon disulfide, diborane, formaldehyde, hydrogen cyanide, hydrogen sulfide, nitric acid, phosgene, sulfur dioxide, tungsten hexafluoride
Explosives	TNT, PETN
<b>2.5–4 <math>\mu\text{m}</math></b>	
TICs	HBr, HCl, HF

- (1) *Sensitivity*. Detection sensitivity is a key indicator of overall sensor performance and relates to the minimum gas concentrations that are reliably detected. A good sensitivity enables detecting CWAs or TICs before the concentration rises to dangerous levels, monitoring at low levels for long-term exposure problems, and determining when an attack site is safe to reenter.
- (2) *Specificity*. Specificity, i.e., the ability to distinguish between different CWAs, is important for first responders in order to provide appropriate treatments subsequent to the exposure. Specificity yields information not only about *how much* of a toxic gas is present but also *which* gas is present.
- (3) *Probability of false positives (PFP)*. This number represents the fraction of measurements that falsely indicate that a toxic gas is present when in reality it is not. Such false alarms often arise from interfering gases that might also be present in the indoor or outdoor environments and typically represent the most significant operational difficulty for field-deployed sensors. A very low PFP is desirable since false alarms cause substantial and expensive disruption in the normal routine of those at the measurement site.
- (4) *Probability of false negatives (PFN)*. This number reflects the fraction of measurements that falsely indicate that a toxic gas is *not* present even though it is present at or above the set threshold level. A low PFN is desired in order to prevent unknown exposure to toxic air.
- (5) *Response time*. Near real-time functionality (response time  $\leq 60$  s) is necessary to provide warnings that are useful for protecting people by isolating locations under attack and evacuating attack sites.
- (6) *Recovery time*. This parameter reflects the time that a sensor requires to recover from a high reading, whether after an exposure to CWAs and/or TICs or a false read-

ing prompted by the presence of an interfering gas.

Designing a sensor to simultaneously satisfy these standards requires quantitative understanding of the sensor's operational characteristics as well as the nature of interferences expected in a realistic environment and their impact on the sensor's operational characteristics.

## B. Required instrument sensitivity

The required sensitivity for CWA detection can be determined by the toxicity levels of particular agents, most of which have been reasonably well documented.<sup>3</sup> The concentrations and related health effects for sarin (GB), a typical nerve CWA, are summarized in Table II.

For a 30-min exposure to sarin, the lethal concentration is approximately 575 ppb (parts per 10<sup>9</sup>), or 3.3 mg/m<sup>3</sup>, while the first noticeable health effect (miosis<sup>3,4</sup>) occurs at 33.3 μg/m<sup>3</sup> (5.8 ppb). For the general population, the suggested limit would be 27 ng/m<sup>3</sup> [4.7 ppt (parts per 10<sup>12</sup>)] for an 8-h exposure. Thus, to protect the population from harm in the event of a sarin attack, reasonable design targets for CWA sensors include (1) a sensitivity of approximately 1 ppb (well below the harm threshold for a 30-min exposure), and (2) a measurement time shorter than 1-min to allow reasonable time for isolation or evacuation. The thresholds for harm from the other CWAs are similar.<sup>3</sup>

The CWAs have absorption strengths of  $\sim(3-6) \times 10^{-3}$  (ppm m)<sup>-1</sup> (Fig. 1). For illustration, we use VX as a typical CWA, having a peak absorption of  $2 \times 10^{-3}$  (ppm m)<sup>-1</sup> at 9.6 μm. Consequently, the infrared absorption at 9.6 μm from 1 ppb of VX would be  $2 \times 10^{-8}$  cm<sup>-1</sup>. Thus, detecting CWAs at ppb to sub-ppb levels using optical-absorption techniques requires an absorption measurement capability as low as 10<sup>-8</sup> cm<sup>-1</sup>.

## C. Selectivity in the presence of interferences

Though sensitivity is a key parameter for a trace gas detection sensor, it is the selectivity (the ability to discriminate the target from interferences to avoid false alarms) that becomes the limiting performance factor when the sensors are used in real-world settings. In these environments, the ambient air is often heavily contaminated with potential interferences.

Traditionally, optical-absorption spectroscopy sensors avoid the effect of interferences by measuring absorption either at a single wavelength or over a narrow wavelength region where the target gas absorbs, but the other gases in the sample do not absorb. This approach has been successful for

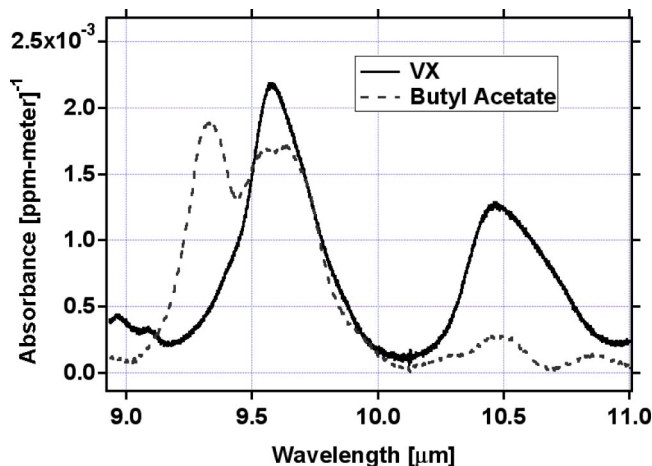


FIG. 2. IR-absorption spectra of VX and a potentially interfering species, butyl acetate.

the detection of smaller molecules in relatively clean samples, where the target gas spectra are sharp and the potential interferences are minimal. However, because CWAs and a majority of interferences that are encountered in realistic air samples are relatively large polyatomic molecules, their IR spectra are characterized by broad absorption features as seen from Fig. 2 that shows the infrared-absorption spectrum of VX and an interferent, butyl acetate. The spectra are several hundred nanometers wide, which is typical of CWAs and interferences, and overlap significantly between 9.5 and 9.9 μm. Since the targets and interferences absorb the probe light at many of the same wavelengths, selective spectroscopic detection of the target requires the acquisition of the spectrum over a broad wavelength range followed by quantitative decomposition into the contributing spectral signatures of the targets and interferences. Thus optical-absorption sensors that operate over a narrow wavelength range would not be able to adequately distinguish these two species.

A sensor's selectivity is typically explained quantitatively through the PFP (or false alarm rate). For a sensor that has a 1-min measurement time, a reasonable design target is to achieve a PFP less than  $2 \times 10^{-6}$ , which corresponds to a false alarm rate of <1 per year.

## D. Photoacoustic spectroscopy

As described, sensors need to detect optical absorptions as small as 10<sup>-8</sup> cm<sup>-1</sup>. There are a number of optical techniques that permit measurements of such small optical absorptions, the most common of which are long path absorption measurements (e.g., multipass cells and cavity ring-down spectroscopy<sup>5</sup>) and calorimetric techniques (e.g., photoacoustics<sup>6</sup>). In this paper, we do not compare the relative merits of various techniques, but we use the example of L-PAS because reliable instruments based on this technique are commercially available for ppb and sub-ppb detection of a variety of relevant trace gases and because it meets the sensitivity requirements as explained in Sec. II B.<sup>7-10</sup> L-PAS is often used<sup>11</sup> with high-power CO<sub>2</sub> lasers that provide (1) wide tunability necessary for measuring CWAs in the presence of interferences, (2) high resolution for distinguishing

TABLE II. Summary of allowable sarin dose (Ref. 3) for different health effects.

Health effect	Dose	Remarks
Lethal (50%)	100 mg min/m <sup>3</sup>	Resting
Incapacitation (50%)	75 mg min/m <sup>3</sup>	Resting
Miosis	1 mg min/m <sup>3</sup>	
Occupational limit	48 μg min/m <sup>3</sup>	8 h/day, 40 h/week, 40 yr
General population	12.96 μg min/m <sup>3</sup>	

sharp spectral features, and (3) an excellent spectral overlap with the wavelength region where most CWAs and many TICs absorb. Though L-PAS is used for illustrative purposes, the analysis presented here is independent of the specific absorption measurement technique, as discussed in the concluding section of this paper.

L-PAS involves absorption of the modulated laser radiation followed by deactivation of the excited molecule via collisions, which convert the absorbed energy into periodic local heating at the modulation frequency, and generate acoustic waves that can be monitored using low-noise microphones.<sup>9–16</sup>

The photoacoustic signal  $S$  in volts is<sup>7</sup>

$$S = S_m P C \alpha, \quad (1)$$

where the microphone sensitivity  $S_m$  is in units of V/Pa, the power  $P$  is in watts, the absorption coefficient  $\alpha$  is in  $\text{cm}^{-1}$ , and the cell factor  $C$  has units of  $\text{Pa cm}^{-1} \text{ W}$ . The photoacoustic signal is linearly proportional to the incident laser power and absorption coefficient at the laser wavelength. Thus, photoacoustic detection of trace-gases-derives sensitivity benefit from the use of as much laser power as is appropriate. To first order, L-PAS is a zero base line technique (i.e., if the gases that are present do not absorb the light, then the transducer yields no signal) and is typically linear over five orders of magnitude, and thus shows magnificent dynamic range.<sup>17</sup>

### III. SIMULATION OF L-PAS CWA SENSOR: SENSITIVITY, PFP, AND PFN EVALUATION

A model of a tunable  $\text{CO}_2$  L-PAS sensor was created using (1) characteristics of an actual field-deployed unit and the spectral information of relevant CWAs and TICs, and (2) potential interferents that might be present.

#### A. The field-deployed sensor

The field-deployed sensor's photoacoustic cell and detection have the following characteristics:

- (1) The optical window materials are chosen to have very low optical-absorption loss in the wavelength regions of interest.
- (2) The photoacoustic cell is operated in a longitudinal resonant mode at  $\sim 2$  kHz, and the laser radiation is amplitude modulated at the resonant frequency.
- (3) The optical windows are attached to the photoacoustic cell through a transition region of much larger diameter and much shorter length than the photoacoustic cell. Thus the resonant frequency of the window attachment chamber is much different from the modulation frequency and is nonresonant. Thus the acoustical signal created by the residual optical absorption in the optical window is not resonantly amplified. There is, furthermore, a substantial acoustical impedance mismatch between the window attachment sections and the photoacoustic cell. The nonresonant nature of the window attachment sections, the large impedance mismatch between the window attachment chambers and the photoacoustic cell, and the use of ultralow loss window mate-

rials result in negligible photoacoustic signal contribution from windows to the signal arising from optical absorption from the gases present in the photoacoustic cell. Finally the window absorption signals, small as they are, are relatively independent of the laser wavelength. Thus, the measurement of the gaseous sample at multiple laser wavelengths permits an almost complete elimination of the window noise problem.

- (4) The photoacoustic cell is operated at a constant temperature of  $42^\circ\text{C}$  and a pressure of near 760 Torr to minimize problems that may arise from changing the temperature or pressure.
- (5) When detecting photoacoustic signal, the deployed sensor measures both the in-phase and out-of-phase components of the signal at all wavelengths. Thus, the sensor keeps track of both the amplitude and the phase of the photoacoustic signal.

The model derived from an actual field-deployed sensor (Sec. III B) was then used repeatedly to simulate CWA detection in the presence of interferences to yield statistics that could be used to estimate the L-PAS sensor's sensitivity, PFN, and PFP. The model incorporates the stochastic nature of sensor instrumentation by adding appropriate noise to the simulated L-PAS spectrum, while the stochastic nature of the interference composition is accounted for by varying the calculated contamination in different air samples. The model presented below simulates sensor performance as a function of three parameters:

- (a) spectral range available from the laser,
- (b) the stochastic noise characteristics of an actual L-PAS sensor, including floor noise, precision, and integration time, and
- (c) list of targets and probable interferences with their expected concentrations and their quantitative spectra (i.e., the spectral libraries).

#### B. Model: The sensor

The sensor model is derived from actual performance characteristics of a practical field instrument that measures ambient ammonia in the presence of interferences using a line tunable  $\text{CO}_2$  L-PAS sensor. This sensor<sup>7,8</sup> uses a  $^{13}\text{CO}_2$  laser with 5 W of average output power operating on its  $10R(18)$  transition near  $10.784 \mu\text{m}$  to interrogate ammonia's strong  $^2Q_6(6)_a$  transition. Interferences from  $\text{CO}_2$ ,  $\text{H}_2\text{O}$  continuum, and window absorptions are subtracted by switching to neighboring laser lines, yielding a replicate precision<sup>8</sup> of 32 ppt. This detectivity corresponds to a minimum detectable fractional absorbance of  $8.8 \times 10^{-9}$ , and a minimum detectable absorption coefficient of  $9.6 \times 10^{-10} \text{ cm}^{-1}$ , thereby satisfying the sensitivity requirements (see Sec. II B). The line-switching algorithm can be extended over many laser lines and combined with linear pattern recognition<sup>11</sup> to detect many species in the presence of a vast majority of interferences encountered in contaminated outdoor or indoor air. From the measurements with clean air<sup>8</sup> we derive the stochastic instrument noise to be 0.2% of the signal amplitude.

TABLE III.  $^{13}\text{CO}_2$  L-PAS sensor interference list.

Species	Concentration (ppb)	Species	Concentration (ppb)	Species	Concentration (ppb)
H <sub>2</sub> O	40 000 000	Formaldehyde	400	Apinene	60
Ethylene glycol	491	Ozone	15	Acrolein	11
Toluene	2 382	TCTFE	3	2butanone	42
CO <sub>2</sub>	550 000	pDCB	13	Freon12	370
Ethanol	146	Butanol	21	Isobutanol	2
Ammonia	22	2butoxyethanol	15	TMB	17
Isopropanol	212	2ethylhexanol	8	dlimonene	23
Methanol	16	Benzene	34	1,3-butadiene	5
p-xylene	649	Trichloroethane	148	oDCB	2
Acetic acid	92	Styrene	14	MTBE	13
m-xylene	649	Naphthalene	71	Butane	33
Ethyl benzene	252	Ethylene	10	Freon11	28
Ethyl acetate	16	Chloroethane	20	o-xylene	16
Texanol	25	Acrylonitrile	11	EEACET	2
Butyl acetate	14	Propylene	10	Chloroform	38

### C. Model: Air composition and spectral library compilation

Because interferences play an important role in determining the sensor performance in the field, we simulate realistic measurement conditions by developing a model of heavily contaminated air that contains a number of trace constituents of anthropogenic and biogenic origin. For example, outdoor air, even in unpolluted areas, contains CH<sub>4</sub>, higher alkanes, NO<sub>x</sub>, SO<sub>x</sub>, NH<sub>3</sub>, O<sub>3</sub>, CO, and CO<sub>2</sub>. Urban polluted air contains fuel vapors, numerous VOCs resulting from incomplete combustion in car engines and smoke stack emissions, as well as an array of intermediates resulting from their atmospheric degradation. Rural air may be contaminated by emissions from agricultural operations leading to significant concentrations of ammonia and sulfur-containing compounds. The sources of the indoor air contamination are even more diverse and include cleaning agents, products of out gassing of common construction materials, paints, solvents, perfumes, food, and tobacco smoke.

Since there is no single reference source that comprehensively quantifies realistic air constituents, we compiled an exhaustive list of documented pollutants. Where both mean and instantaneous (spike) concentration levels are reported in the literature, the higher spike values are chosen to be representative of the highest possible contamination and to serve as a stricter test. For most chemicals, however, only average values over multihour measurement periods are available. To estimate the highest possible spike values, resulting from spills, we use the results of an analytical model,<sup>18</sup> which considers a vapor diffusion process from a point source in a reasonably ventilated indoor area. According to this model, the highest concentration reached in the vicinity (1 m away) of the spill is four times the steady-state value established after the evaporation rate becomes equal to the rate of removal of the vapor via ventilation. Therefore, in the cases where only mean concentrations were reported, we multiplied the highest reported value by a factor of 4 to achieve

the expected spike value. The list includes more than 300 species and represents, possibly, the most complete compilation of published data on the topic and, thus, is the best practical starting point for evaluating a sensor's performance in realistic air. (The complete list of documented compounds, their largest reported concentrations, and references to original literature sources are not reported here, but may be obtained from the authors.) We have also assembled a digital quantitative, high-resolution (0.25 cm<sup>-1</sup>) library of absorption spectra of each of these potential interferences by using published databases<sup>2</sup> and commercially available databases.

This list of some three hundred species is impractically large and is truncated for the present analysis by removing a chemical from further consideration if

- (1) it has been reported in indoor air in negligible quantities such that its optical absorption is less than the equivalent of 1 ppb of sarin (1 ppb of sarin is used as a cutoff since this number is well below the harm threshold of 5.8 ppb for a 30-min exposure as seen in Sec. II), and
- (2) if the species does not absorb light appreciably at any wavelength within the range of the carbon dioxide laser, and therefore would not interfere with a target gas even if present in substantial quantities.

Table III lists 45 species that meet the criteria and are part of the interference library.

Figure 3, showing the absorption spectra of eight target nerve agents and surrogates at wavelengths accessible with  $^{12}\text{CO}_2$  and  $^{13}\text{CO}_2$  lasers, indicates that the absorption spectrum of DIMP (a relatively harmless surrogate for nerve agents) has excellent overlap with the available laser transitions from a  $^{13}\text{CO}_2$  laser. Consequently, the modeling was performed for a  $^{13}\text{CO}_2$  L-PAS sensor for DIMP detection. The libraries of spectra were converted into the spectra specific to a  $^{13}\text{CO}_2$  L-PAS by evaluating the absorption coefficients at the 87 discrete  $^{13}\text{CO}_2$  laser wavelengths in the 9.6–11.5- $\mu\text{m}$  range. The spectral signatures of the 45 interferents

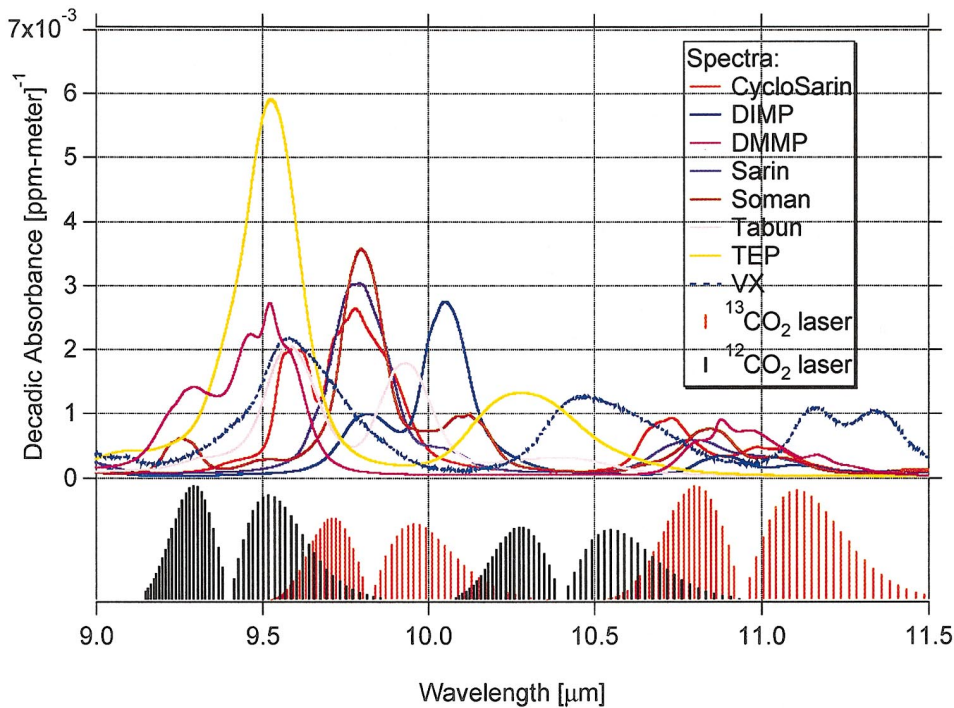


FIG. 3. (Color) Spectra of nerve agents and <sup>12</sup>CO<sub>2</sub> and <sup>13</sup>CO<sub>2</sub> laser wavelengths

were then used to evaluate matrix elements involved in the least-squares fit (LSF) spectral decomposition to be described in Sec. III D.

**D. The simulation model: Spectral decomposition algorithm**

In realistic air both targets and interferents contribute to the measured L-PAS spectrum. The mathematical problem of decomposition of a multicomponent spectrum may be solved using the LSF technique. Using Eq. (1), a L-PAS spectrum of the air containing multiple contaminants can be simulated.

In the gas mixture the absorption coefficient  $\alpha_{\lambda_j}$  at each wavelength  $\lambda_j$  is given by

$$\begin{aligned} \text{Absorption coefficient}|_{\lambda_j} = \alpha_{\lambda_j} &= \sum_{i=1}^{\# \text{ species}} \alpha_{i,\lambda_j} \\ &= \sum_{i=1}^{\# \text{ species}} X_i \sigma_{i,\lambda_j}, \end{aligned} \tag{2}$$

where  $\sigma_{i,\lambda_j}$  is the absorbance for species  $i$  at wavelength  $\lambda_j$ , and  $X_i$  is the mole fraction of the species  $i$ . According to Eq. (1), if  $S_{\lambda_j}$  is the measured photoacoustic signal and  $P_{\lambda_j}$  is the measured laser power at a given wavelength, the L-PAS spectrum (the set of values of absorption coefficients  $\alpha_{\lambda_j}$  versus wavelength  $\lambda_j$ ) may be obtained using Eq. (3),

$$\alpha_{\lambda_j, \text{measured}} = \frac{S_{\lambda_j}}{S_m P_{\lambda_j} C}. \tag{3}$$

Combining Eqs. (2) and (3) and noting that in any real sensor a measured absorption coefficient  $\alpha_{\lambda_j, \text{measured}}$  inevitably contains instrumentation noise yield

$$\alpha_{\lambda_j, \text{measured}} = \sum_{i=1}^{\# \text{ species}} X_i \sigma_{i,\lambda_j} + \text{Noise}_{\lambda_j}. \tag{4}$$

The L-PAS spectrum of a multicomponent mixture is a linear combination of the known spectra of individual constituents, with the coefficients being the mole fractions of individual components  $X_i$  plus a stochastic term due to instrumental noise of the sensor. During measurements, the sensor acquires a L-PAS spectrum of a sample. The unknown mole fractions for each species are subsequently determined via the linear least-squares fit, i.e., from the requirement that the sum of the squares of the differences between measured and simulated absorption coefficients (so-called merit function  $\chi^2$ ) over all wavelengths is minimum,

$$\chi^2 = \sum_j^{\# \text{ lines}} \left( \alpha_{\lambda_j, \text{measured}} - \sum_{i=1}^{\# \text{ species}} X_i \sigma_{i,\lambda_j} \right)^2 = \min. \tag{5}$$

Using vector-matrix notation, Eq. (4) may be represented as

$$\begin{bmatrix} \sigma_{\lambda_1,1} & \sigma_{\lambda_1,2} & \cdots & \sigma_{\lambda_1,M} \\ \sigma_{\lambda_2,1} & \sigma_{\lambda_2,2} & \cdots & \sigma_{\lambda_2,M} \\ \vdots & \vdots & \ddots & \vdots \\ \sigma_{\lambda_N,1} & \sigma_{\lambda_N,2} & \cdots & \sigma_{\lambda_N,M} \end{bmatrix} \begin{bmatrix} X_1 \\ X_2 \\ \vdots \\ X_M \end{bmatrix} + \begin{bmatrix} n_1 \\ n_2 \\ \vdots \\ n_M \end{bmatrix} = \begin{bmatrix} \alpha_1 \\ \alpha_2 \\ \vdots \\ \alpha_M \end{bmatrix}. \tag{6}$$

Equation (7) gives the LSF values of individual mole fractions  $X_i$  which are the solutions of Eq. (5),

$$\begin{array}{c} \text{Mole fractions} \\ \left\{ \begin{array}{c} X_1 \\ X_2 \\ \vdots \\ X_M \end{array} \right\} = \left[ \begin{array}{cccc} \vec{\sigma}_1 \vec{\sigma}_1 & \vec{\sigma}_2 \vec{\sigma}_1 & \cdots & \vec{\sigma}_N \vec{\sigma}_1 \\ \vec{\sigma}_1 \vec{\sigma}_2 & \vec{\sigma}_2 \vec{\sigma}_2 & \cdots & \vec{\sigma}_N \vec{\sigma}_2 \\ \vdots & \vdots & \ddots & \vdots \\ \vec{\sigma}_1 \vec{\sigma}_M & \vec{\sigma}_2 \vec{\sigma}_M & \cdots & \vec{\sigma}_N \vec{\sigma}_M \end{array} \right]^{-1} \\ \times \left[ \begin{array}{cccc} \sigma_{\lambda_1,1} & \sigma_{\lambda_2,1} & \cdots & \sigma_{\lambda_N,1} \\ \sigma_{\lambda_1,2} & \sigma_{\lambda_2,2} & \cdots & \sigma_{\lambda_N,2} \\ \vdots & \vdots & \ddots & \vdots \\ \sigma_{\lambda_1,M} & \sigma_{\lambda_2,M} & \cdots & \sigma_{\lambda_N,M} \end{array} \right] \left\{ \begin{array}{c} \alpha_1 \\ \alpha_2 \\ \vdots \\ \alpha_M \end{array} \right\}. \end{array} \quad (7)$$

The LSF algorithm for an ideal sensor (with zero noise) yields the concentration of the target species even in the presence of multiple interferences if (1) a quantitative L-PAS spectral library for all expected targets and interferences exists, (2) the number of wavelengths used for the measurement is greater than the number of absorbing species, and (3) the individual spectra are linearly independent. A stochastic noise term in Eqs. (5) and (6) introduces error in the measured absorption coefficients and consequently in the best-fit values of  $X_i$  obtained from Eq. (7). Sensor model simulations based on Eqs. (4)–(7), described below, reveal quantitative limitation imposed by stochastic noise on the performance of practical sensors.

### E. Sensor stochastic noise

To quantitatively analyze the performance of L-PAS for CWA detection (sensitivity, specificity, PFN, and PFP), one needs to understand the sources and evaluate the magnitude of noise in the detection scheme of the actual L-PAS-based instrumentation. L-PAS sensor has two critical transducers that introduce noise: a microphone measuring the photoacoustic signal  $S_{\lambda_j}$  and a power meter measuring the laser power  $P_{\lambda_j}$ . Outputs from these two sensors are used to obtain the absorbance values  $\alpha_{\lambda_j}$  using Eq. (2). For constant ambient conditions of the sample (temperature, pressure) in the photoacoustic cell, the uncertainty in the measured absorption coefficient arises from the sensor noise.

The sensor noise is a sum of noise independent of signal amplitude (the floor noise) and noise proportional to the total measured PAS signal amplitude scaled by the instrument precision  $\beta$ ,

$$\text{Noise} = \sqrt{n_{\text{floor}}^2 + n_{\text{precision}}^2} \quad (8)$$

$$n_{\text{precision}} = S_{\lambda_j} \beta. \quad (9)$$

The fundamental noise floor on photoacoustic detection arises from the Brownian noise created by the gas molecules in the photoacoustic sensor and is given by an equivalent absorbed optical power of about  $10^{-11}$  W Hz<sup>-1/2</sup> at room temperature.<sup>19</sup> For actual instruments, the lowest possible floor noise value is determined by the specifications of the transducers, i.e., the power meter and the microphone. The instrument precision is, in turn, determined by the quality, i.e., linearity, digitization resolution, etc., of the signal con-

ditioning and data acquisition electronics. Floor noise and the precision values were determined from a field-deployed L-PAS sensor, and yielded a precision of approximately  $\beta = 0.002$  with roughly Gaussian stochastic properties and no obvious systematic components. At this level, the precision noise exceeds the floor noise by almost three orders of magnitude and the latter can thus be disregarded.

Thus, an absorption spectrum of an air sample containing a particular mixture of trace gases (both targets and interferences) acquired with CO<sub>2</sub> L-PAS sensor may be simulated using Eq. (4) with the noise term governed by limited sensor precision,

$$\alpha_{\lambda_j} = \sum_{i=1}^{\# \text{ species}} X_i \sigma_{i,\lambda_j} (1 + \beta \text{gauss}), \quad (10)$$

where  $\beta$  is the sensor precision, and gauss is the function generating Gaussian-distributed random numbers with a mean value of 0 and variance (one standard deviation) of 1. If there is no instrumental noise,  $\beta=0$ , i.e., no stochasticity, the best-fit values  $X_{i \text{ best fit}}$  practically coincide with the values of  $X_i$  used to simulate air in Eq. (10). As the stochastic instrumental noise is added, the LSF produces values of  $X_{i \text{ best fit}}$  which differ from the values  $X_i$  from Eq. (10). The statistical distribution of this difference allows one to quantitatively measure the sensor performance.

## IV. RESULTS OF THE SIMULATION MODEL: DETECTION OF CWA

Simulations can now be performed using the analytical model to predict the PFN, PFP, and sensitivity for the sensor. The steps leading to the generation of ROC curves are the following:

- generate a synthetic photoacoustic spectrum of the “contaminated air” by adding up the absorption spectra of all interferences at their highest concentrations and imposing a stochastic noise according to Eq. (10);
- determine the best-fit mole fraction of a particular target species (DIMP)  $X_{\text{DIMP-best fit}}$  by the LSF analysis of the synthetic spectrum using Eq. (7) (with all involved matrix elements evaluated using the absorbance values  $\sigma_{i,\lambda_j}$  from spectral library); and
- repeat the simulation for a large number of times ( $\sim 10^5$ ), each time generating a different spectrum due to the stochastic nature of the gauss function. The resulting distribution of the best-fit concentration values  $X_{\text{DIMP-best fit}}$  yields instrument sensitivity, PFP, and PFN versus detection threshold and challenge, respectively.

### A. Sensitivity

The simulation was first performed for the case of 10-ppbv (parts per 10<sup>9</sup> by volume) DIMP challenge in clean, dry air yielding a histogram of results with a deduced average measurement of 10.00 ppbv and a standard deviation of 20 ppt. These results agree well with the field sensor tests for ammonia, which has a similar peak absorption coefficient as DIMP. The simulation for the 10-ppbv DIMP was repeated

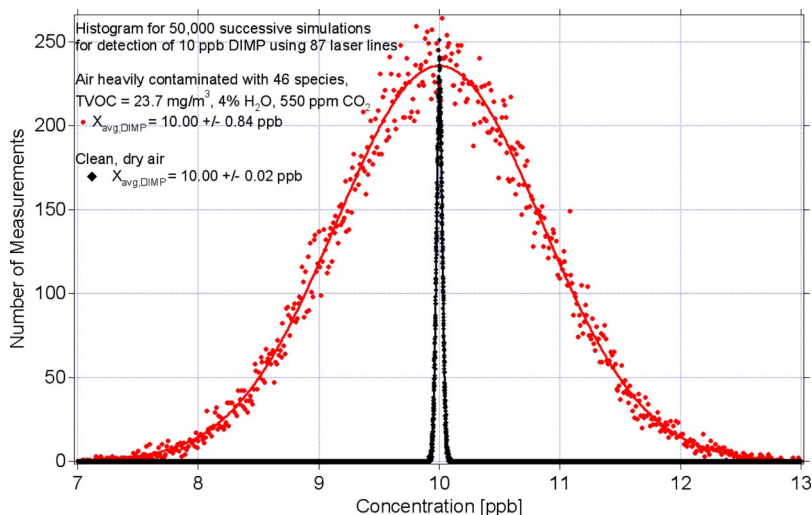


FIG. 4. Histogram of simulations of 10-ppbv DIMP detection in contaminated air overlaid with the histogram from simulated measurements of 10-ppbv DIMP in clean, dry air.

with interferences from a worst-case air model (Table III), including high humidity (4% H<sub>2</sub>O), 550-ppm CO<sub>2</sub>, and high VOC density of 23.7 mg/m<sup>3</sup>, which is nearly two orders of magnitude greater contamination than that in nominal conditions. For this simulation, the average deduced value is 10.00 ppbv with a standard deviation of 840 pptv (parts per 10<sup>12</sup> by volume), illustrating the impact of the interfering species. The histograms of the results for the two simulations are overlaid in Fig. 4. The impact of the interferences on the measurement precision is due to the increased absorption coefficients measured by the sensor leading to an increase in their absolute uncertainty due to limited instrumental precision [Eq. (10)], which leads to an increased uncertainty in the results of the spectral decomposition algorithm.

**B. Probability of false positives**

To determine the sensitivity and detection threshold versus PFP (ROC curve), the simulations must be performed with the interferences present but the target gas absent. The standard deviation of this distribution is the sensitivity. The PFP (for a given threshold) is determined from the same

distribution by evaluating how often the sensor mistakenly yields a reading above a predetermined threshold. The simulations with the “worst-case” contaminated air and no DIMP yielded a histogram (Fig. 5) centered at 0.01 ppbv, with a standard deviation of 850 pptv, which defines the instrument’s sensitivity. The PFP at a particular alarm threshold is determined from the histogram as the number of readings above the threshold normalized by the total number of simulations. For example, for a threshold of 1.5 ppbv, the PFP is the ratio of the integrated area under the curve above 1.5 ppbv (shown as A<sub>1</sub> on the plot) and the total integrated area (shown as the sum of A<sub>1</sub> and A<sub>2</sub> on the plot), indicating that 7.7% of the readings will surpass the threshold and thereby falsely set off an alarm. Similarly, for an alarm threshold of 4.15 ppbv, only 1 in every 10<sup>6</sup> sensor readings will falsely trigger the alarm when no DIMP is present. And, of course, for an alarm threshold of 0 ppbv, all measurements will set off the alarm, yielding a PFP of 100%.

To obtain the ROC curve, i.e., the PFP as a function of different thresholds, the process is repeated for different alarm levels. The result, plotted in Fig. 6, indicates that as

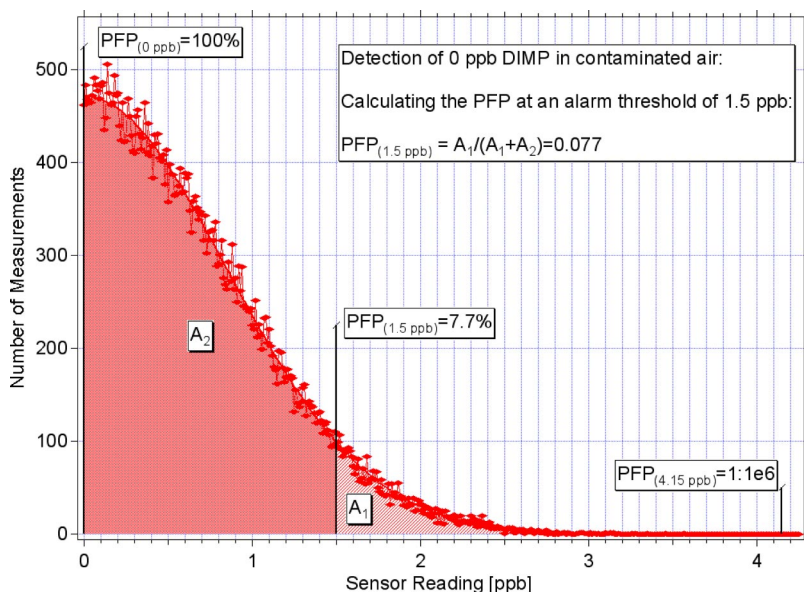


FIG. 5. Simulated sensor response to 0-ppbv DIMP in contaminated air. The PFP for an alarm threshold of 1.5 ppbv is the area A<sub>1</sub> divided by the sum of areas A<sub>1</sub> and A<sub>2</sub>.

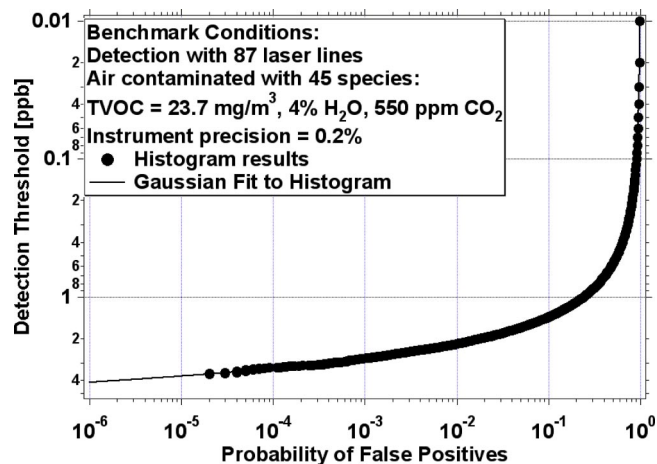


FIG. 6. Plot of PFP vs detection threshold for detecting DIMP from simulated measurements of heavily contaminated air with TVOC=23.7 mg/m<sup>3</sup>, 4% H<sub>2</sub>O, and 550-ppm CO<sub>2</sub> (a total of 45 interferences) and using 87 laser lines from a <sup>13</sup>CO<sub>2</sub> laser. A PFP of 1 × 10<sup>-6</sup> is achieved for a detection threshold of 4.15 ppb.

the threshold level increases the PFP decreases rapidly, and for the 4-ppb threshold the PFP reaches the value of ~10<sup>-6</sup>.

**C. Probability of false negatives**

To evaluate the sensor PFN the instrument performance must be modeled when challenging the system with DIMP at a level exceeding the alarm threshold and determining the normalized portion of the histogram (area A<sub>1</sub> divided by area A<sub>1</sub>+A<sub>2</sub>) below an alarm threshold (area A<sub>1</sub> divided by area A<sub>1</sub>+A<sub>2</sub>). Figure 7 illustrates PFN calculation for the “worst-case” air. With an alarm threshold of 1 ppbv and a challenge of 2-ppbv DIMP, the distribution reveals that 11.3% of the sensor readings will falsely indicate that DIMP is not present.

**D. Sensitivity, PFP, and PFN**

By evaluating the PFN at a range of alarm thresholds, the PFP curve from Fig. 6 can be color coded to reflect PFP and PFN simultaneously, as shown in Fig. 8. Combined dis-

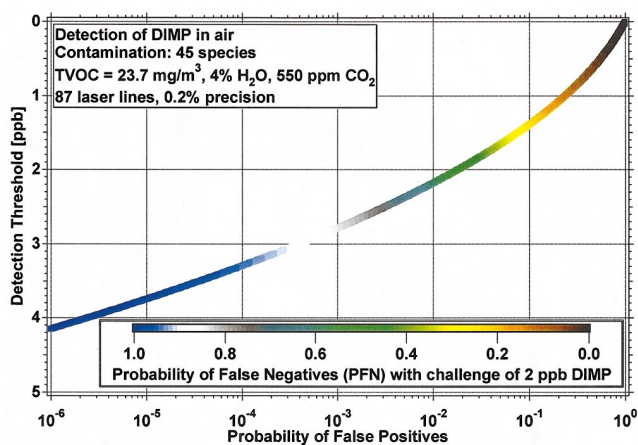


FIG. 8. (Color) Plot of PFP and PFN vs detection threshold for detecting DIMP from simulated measurements of heavily contaminated air with TVOC=23.7 mg/m<sup>3</sup>, 4% H<sub>2</sub>O, and 550-ppm CO<sub>2</sub> (a total of 45 interferences) and using 87 laser lines from a <sup>13</sup>CO<sub>2</sub> laser.

play such as the one in Fig. 8 represents an important tool that allows users to specify alarm settings based on the priorities of their applications.

**V. IMPROVEMENTS IN SENSITIVITY FOR DETECTION OF CWA**

The simulation model provides the tools for exploring ways by which the CWA detection performance may be improved or for testing the limits of the instrument usability in the case of extreme situations. The model has three input parameters: air composition, instrument precision, and laser spectral coverage. The effects of improving the precision of the photoacoustic detection and varying the total volatile organic compound interference load were studied. We have not studied the effects of varying the spectral coverage because the tuning range afforded by a CO<sub>2</sub> laser is fixed.

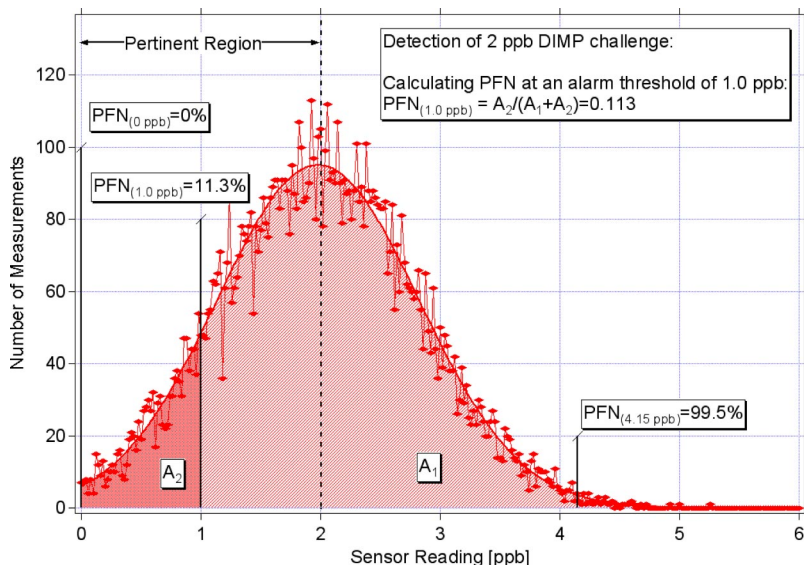


FIG. 7. Simulated sensor response to 2-ppb DIMP in contaminated air. The PFN obtained by analyzing the number of sensor readings that are below a particular alarm threshold even though DIMP is present at higher concentrations.

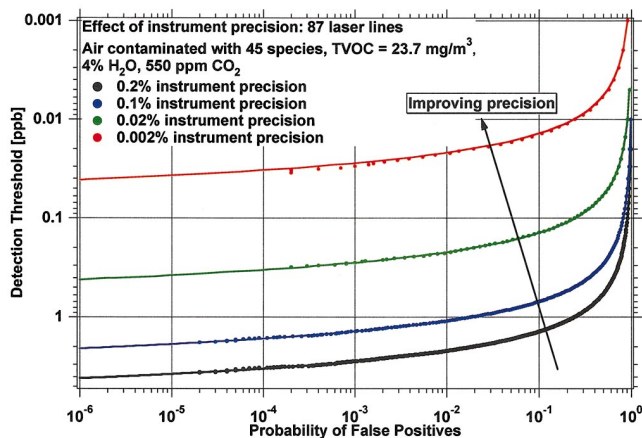


FIG. 9. (Color) Simulated ROC curves illustrating improvement in the PFP of L-PAS detection with improving the precision of the sensor.

**A. Improving operational noise characteristic of the photoacoustic sensor**

As can be deduced from the earlier discussion, a limitation to the sensitivity for a desired PFN and PFP comes from the “noise” from the photoacoustic sensor. As described above, the limiting factor for the field-deployed L-PAS sensor was its precision, which is the result of the instrument’s 10-bit digitizer (9 bits plus sign). The 9-digitization bits give a maximum resolution of 1:512, or approximately 0.002 times the maximum signal for a precision  $\beta=0.2\%$ . By using a 16-bit digitizer (15 bits plus sign) we can improve the resolution to 1:32 768, yielding  $\beta=0.003\%$ . With this improvement, the noise due to limited precision is still larger than the floor noise, but only by a factor of 10. The improvement in the overall system performance that can be obtained by reducing the total noise is shown in Fig. 9, which plots the results for different values of precision. For example, an improvement of a factor of 60 in precision (going from a 10-bit digitizer to a 16-bit digitizer) will improve the detection sensitivity by about the same factor, i.e., 60.

**B. Reducing the total level of volatile organic compound interference**

Figure 10 shows the results of simulations for the worst-case contaminated air, with a total VOC (TVOC) density of  $23.7 \text{ mg/m}^3$ , and for air samples with  $2\times$  and  $10\times$  less contamination. As the total contamination decreases, the sensor’s selectivity improves. For the worst-case contamination, a PFP of  $1 \times 10^{-6}$  can be achieved for a detection threshold of 4.15 ppb. Reducing the contamination by a factor of 10– $2.37 \text{ mg/m}^3$  lowers that threshold to 0.74 ppb.

**C. Increasing the density of sampling wavelengths**

The simulation reported here has been carried out using available laser wavelengths from a  $^{13}\text{CO}_2$  laser that provides discrete tuning of laser wavelengths, which are separated by approximately  $1\text{--}2 \text{ cm}^{-1}$ . Since the performance of such an optical sensor depends on the quality of shape information about the total optical absorption presented by the gas sample, it stands to reason that sampling at additional wave-

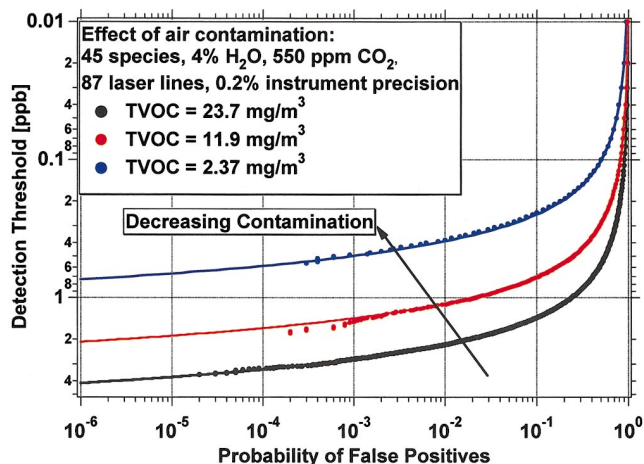


FIG. 10. (Color) Simulations demonstrating the impact of reducing contamination on the performance of the sensor. Typical indoor air has a total VOC (TVOC) density of  $<0.5 \text{ mg/m}^3$ .

lengths to fill in the gaps between the fixed natural frequencies of the  $^{13}\text{CO}_2$  laser should help. We have explored this improvement through interspersing the  $^{13}\text{CO}_2$  laser wavelengths with notional additional wavelengths to increase the density by factors of 2 and 5, i.e., reducing the spacings between the available sampling wavelengths by factors of 2 and 5, respectively. The simulation carried out to demonstrate the improvement is shown in Fig. 11. Here, we have analyzed a slightly different case than that analyzed earlier in the paper. We use a TVOC loading of  $4.35 \text{ mg/m}^3$  and 44 of the  $^{13}\text{CO}_2$  laser lines as the reference case. The two additional curves in the figure show the detection threshold versus PFP (and PFN using the color-coding scheme described in connection with Fig. 8) for 88 and 220 sampling wavelengths covering the same spectral region as the 44 wavelength case, but with increased density of lines as described above. The improvement in the performance is remarkable and points to the need for the use of perhaps a continuously tunable laser (in place of the discretely tunable  $^{13}\text{CO}_2$  laser described in this simulation) for creating the CWA and TIC sensor with improved performance.

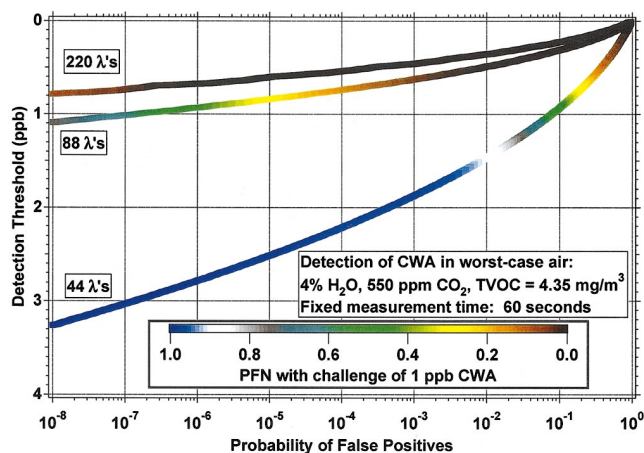


FIG. 11. (Color) Performance improvement of the L-PAS sensor by increasing the density of sampling wavelengths.

## VI. CONCLUSIONS

The problem of sensitively detecting CWAs and TICs in the presence of a realistic array of interferences has been analyzed by illustrative use of a L-PAS system. An analytical model for the optical detection of CWAs and TICs has been developed that can be used for *ab initio* calculations of L-PAS to determine optimum designs, and was used to evaluate the sensitivity, PFP, and PFN. Ultimately, the performance of a L-PAS sensor depends on the availability of high-power broadly tunable laser sources, high precision instrumentation, and quantitative spectral libraries.

This L-PAS performance (sensitivity and PFP) can be improved substantially through systematic optimization that includes improvements in the performance of instrument components and design, for example, using higher laser output power and tuning range, as well as systematic engineering improvements, such as using better precision analog-to-digital (A/D) converters, transducers, and conditioning electronics.

The approach described in this paper may be used for comparing and optimizing the use of other optical detection technologies for the measurement of CWAs and TICs. The vehicle we have chosen is the L-PAS. However, the fundamental property that we measure is the optical absorption. Any other technique that yields the optical-absorption signatures, such as long path optical-absorption measurements, cavity ring-down spectroscopy or Fourier transform infrared (FTIR), is also equally well described by the analysis presented in this paper. In carrying out the analysis for other modalities of absorption measurements, the photoacoustic signal  $S$  that is directly proportional to the absorption can be substituted by the actual measured absorption values. The appropriate “noise” for the system must be added to these measurements to derive a stochastically dependent variation of sensitivity with PFP and PFN.

It is clear that the discrete tuning characteristics of the CO<sub>2</sub> laser is probably not optimum for obtaining detailed information about the shape of absorption in the presence of interferences. The better the shape information, the better will be the possibility of rejection of interferences. Our studies show that by increasing the density of absorption sampling wavelengths beyond what is available from the <sup>13</sup>CO<sub>2</sub> laser, for example, through the use of nonlinear mixing techniques or use of tunable semiconductor lasers, the detection threshold can be improved significantly without sacrificing PFP. Thus, we suggest that using continuously tunable laser sources in place of the discretely tunable sources would lead to considerable performance improvement. However, we should also note that the density of sampling wavelengths need not be any greater than what is required to resolve the absorption features of a light molecule at the gas pressure in the photoacoustic cell (at or near 760 Torr).

Finally, the model presented here assumes that the molecular absorption cross sections and absorption wavelengths are accurately known. However, in practice this may not be the case, although for the purposes of creating the simulation

model and optimizing the CWA sensor performance the uncertainty does not play a major role. Therefore, in our current work leading to experimental validation of the simulation model, we measure the actual absorption coefficients of the various constituents of the gas sample individually at the specific CO<sub>2</sub> laser wavelengths used in the experiment. This procedure will provide the “most accurate” absorption coefficients of the components of the “soup” at the precise CO<sub>2</sub> laser wavelengths, thus eliminating problems arising from the experimental uncertainty in the spectra obtained from other sources. These measured values of the absorption cross sections will then be used in the simulation model to provide a better comparison with future experiments.

## ACKNOWLEDGMENT

This work was supported, in part, through DARPA Contract No. MDA972-02-C-0092 (approved for public release, distribution unlimited).

<sup>1</sup>Protocol for the Prohibition of the Use in War of Asphyxiating, Poisonous or Other Gases, and of Bacteriological Methods of Warfare (1925); Entry into force: 8 February 1928; The Chemical Weapons Convention was opened for signature in Paris, 13 January 1993 and entered into force 29 April 1997.

<sup>2</sup>S. W. Sharpe, R. L. Sams, T. J. Johnson, P. M. Chu, G. C. Rhoderick, and F. R. Guenther, SPIE Proceedings for Vibrational Spectroscopy-Based Sensor Systems (unpublished), Vol. 4577, pp. 12–24.

<sup>3</sup>See for example, *Army Field Manual No. 3-9; Potential Military Chemical/Biological Agents and Compounds*, pp. 19–20 (Headquarters of the Army, Washington, DC, 1990); B. McNamara and L. Leitnaker, *Toxicological Basis for Controlling Emission of GB into the Environment (Edgewood Arsenal Special Publication)* (U. S. Army, Medical Research Laboratories, Edgewood Arsenal, MD, 1971); Department of Health and Human Services, Center for Disease Control, Final Recommendations for Protecting the Health and Safety against Potential Adverse Effects of Long-Term Exposure to Low Doses of Agents: GA, GB, VX, Mustard Agent (H, HD and T) and Lewisite (L), Federal Register, Vol. 53 (1988), pp. 8504–8507.

<sup>4</sup>The first noticeable health effect is miosis, which for sarin includes pinpointing of the pupil of the eye accompanied by runny nose, tightness of the chest, and eye pain.

<sup>5</sup>A. O’Keefe and D. A. G. Deacon, *Rev. Sci. Instrum.* **59**, 2544 (1988); see also J. J. Scherer, J. B. Paul, A. O’Keefe, and R. J. Saykally, *Chem. Rev.* (Washington, D.C.) **97**, 25 (1997).

<sup>6</sup>*Topics in Current Physics: Photoacoustic, Photothermal and Photochemical Processes in Gases*, edited by P. Hess (Springer, Berlin, 1989).

<sup>7</sup>M. B. Pushkarsky, M. E. Webber, O. Baghdassarian, L. R. Narasimhan, and C. K. N. Patel, *Appl. Phys. B: Lasers Opt.* **75**, 391 (2002).

<sup>8</sup>M. B. Pushkarsky, M. E. Webber, and C. K. N. Patel, *Appl. Phys. B: Lasers Opt.* **77**, 381 (2003).

<sup>9</sup>C. K. N. Patel, E. G. Burkhardt, and C. A. Lambert, *Science* **184**, 1173 (1974).

<sup>10</sup>M. Nagele and M. W. Sigrist, *Appl. Phys. B: Lasers Opt.* **70**, 895 (2000).

<sup>11</sup>L. B. Kreuzer, N. D. Kenyon, and C. K. N. Patel, *Science* **177**, 347 (1972).

<sup>12</sup>L. B. Kreuzer and C. K. N. Patel, *Science* **173**, 45 (1971).

<sup>13</sup>P. Repond and M. W. Sigrist, *Appl. Opt.* **35**, 4065 (1996).

<sup>14</sup>A. Miklos, P. Hess, and Z. Bozoki, *Rev. Sci. Instrum.* **72**, 1937 (2001).

<sup>15</sup>S. Schafer, A. Miklos, and P. Hess, *Appl. Opt.* **36**, 3202 (1997).

<sup>16</sup>M. E. Webber, M. Pushkarsky, and C. K. N. Patel, *Appl. Opt.* **42**, 2119 (2003).

<sup>17</sup>A. Schmohl, A. Miklos, and P. Hess, *Appl. Opt.* **41**, 1815 (2002).

<sup>18</sup>P. J. Drivas, P. A. Valberg, B. L. Murphy, and R. Wilson, *Indoor Air* **6**, 271 (1996).

<sup>19</sup>L. B. Kreuzer, *J. Appl. Phys.* **42**, 2934 (1971).